

Solar neutrino background in high-pressure gaseous $^{82}\text{SeF}_6$ TPC neutrinoless double beta decay experiments*

Jiemiao Wang (王杰妙)^{1,2} Hulin Wang (汪虎林)^{1,2†} Dongliang Zhang (张冬亮)^{1,2‡} 

¹PLAC, Key Laboratory of Quark and Lepton Physics (MOE), Central China Normal University, Wuhan 430079, China

²Hubei Provincial Engineering Research Center of Silicon Pixel Chip & Detection Technology, Wuhan 430079, China

Abstract: In this study, the possibility of observing a solar neutrino background in a future neutrinoless double beta decay experiment using a high-pressure gaseous $^{82}\text{SeF}_6$ TPC is investigated. Various contributions are simulated, and possible features that could be used for event classification are discussed; two types of backgrounds are identified. The rate of multi-site background events is approximately 0.63 events/(ton·yr) in a 30 keV ROI window. This background could be effectively reduced to less than 0.0001 events/(ton·yr) (95% C.L.) while maintaining a high signal efficiency of 93% by applying a selection based on the number of clusters and energy of the leading cluster. The rate of the single-electron background events is approximately 0.01 events/(ton·yr) in the ROI. Assuming a reduction factor of 10 for the single-electron background events obtained via the algorithms developed for radioactive background rejection, the total background induced by the solar neutrino would be 0.001 events/(ton·yr), which is sufficiently small for conducting ton-level experiments.

Keywords: neutrinoless double beta decay, SeF₆, high-pressure TPC, solar neutrino

DOI: 10.1088/1674-1137/ad2675

I. INTRODUCTION

The neutrinoless double beta decay ($0\nu\beta\beta$) experiment is currently the only practical experimental method to test the Majorana nature of neutrinos. Even after 75 years of experimental searches since the first attempt in 1948 [1], only null results have been obtained. Stringent limits are set for isotopes, for instance, $T_{1/2} > 2.6 \times 10^{26}$ yr for ^{136}Xe from the KamLAND-Zen experiment [2] and $T_{1/2} > 1.8 \times 10^{26}$ yr for ^{82}Se from the GERDA experiment [3] at a 90% C.L.

The next generation $0\nu\beta\beta$ experiments are aiming to obtain a half-life sensitivity of up to $T_{1/2} \sim 10^{27} - 10^{28}$ yr, corresponding to the effective Majorana mass $m_{\beta\beta} \sim 5 - 20$ meV, below the Inverted Mass Ordering region.

For this type of rare decay processes, background control is crucial. Ideally, experiments would like to achieve "zero background" to maximize the use of the isotopes, which are usually expensive. For a simple counting experiment, the dependence of sensitivity on the expected number of background events, b , is illustrated in Fig. 1. The 95% upper limit is calculated using the Bayesian statistics with a flat prior for signal. Moreover, the discovery significance is calculated following the fre-

quentist definition [4, 5]. The expected limits become almost flat when $b < 0.7$. However, the discovery could be considered as background free if $b < 0.0027$, below which one can claim a "3 σ significance" with a single event being observed. If $b < 0.0011$, an experiment could reach a "5 σ significance" with two observed events. To claim a "5 σ significance" with one observed event, one needs $b < 5.7 \times 10^{-7}$. Keeping the background low is essential for early discovery of a signal if it exists.

The two neutrino double beta decay ($2\nu\beta\beta$) is an intrinsic background that could only be reduced by improving the energy resolution. Other backgrounds come from the cosmic rays and the natural radioactivity in the environment, detector, and working medium. While most of these backgrounds could be suppressed by radio-purity material selection, shielding, or coincidence detection, the neutrino background, due to its weak interaction with materials, could survive and become an important background. As its contribution scales with the medium, it becomes particularly important for large detectors, which is the case for most of the next-generation experiments. Solar neutrino is the main source of the background in the relevant energy range (a few MeV).

Among the many technologies exploited by the next

Received 11 October 2023; Accepted 6 February 2024; Published online 7 February 2024

* Supported in part by the National Natural Science Foundation of China (12105110) and National Key Research and Development Program of China (2022YFA1604703)

[†] E-mail: hulin.wang@ccnu.edu.cn

[‡] E-mail: dzhang@ccnu.edu.cn

©2024 Chinese Physical Society and the Institute of High Energy Physics of the Chinese Academy of Sciences and the Institute of Modern Physics of the Chinese Academy of Sciences and IOP Publishing Ltd

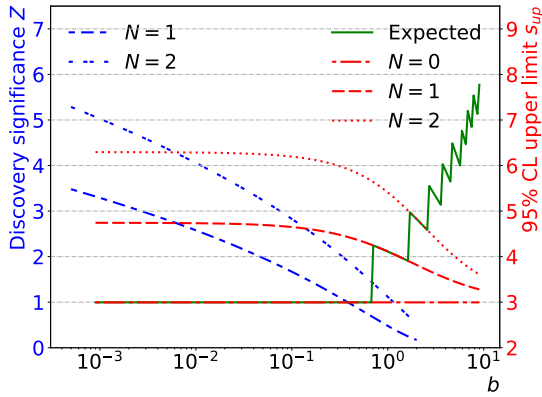


Fig. 1. (color online) Discovery significance Z and upper limit s_{up} at 95% C.L. as functions of b for the cases of zero, one, two, or more events (N) observed in the Region of Interest (ROI). The green solid line depicts the expected limit using the Asimov dataset (median of possible number of observed data).

generation experiments, the high-pressure gaseous Time Projection Chamber (TPC) method has its unique advantages and is developing rapidly. High-pressure gaseous TPCs using ^{136}Xe are explored by NEXT [6] and PandaX-III [7]. The use of $^{82}\text{SeF}_6$ has been discussed in [8, 9], and a dedicated experiment is proposed in [10]. A few advantages make this experimental framework promising: 1) the high $Q_{\beta\beta}$ value of ^{82}Se is above the energy of major radioactive gammas, 2) the low diffusion from the ion drifting allows good tracking, 3) the low noise pixel readout chips could provide excellent energy resolution, and 4) the deep Jinping underground Lab effectively reduces the cosmic background.

Moreover, as the solar neutrino becomes an important background for $0\nu\beta\beta$ experiments, these experiments

could facilitate solar neutrino studies. Both ^{82}Se and ^{19}F have been proposed for solar neutrino studies [11–16]. In the meantime, an electronegative gaseous TPC with high Fluorine content is also proposed for Dark Matter searches [17–19].

The focus of this study is to investigate the solar neutrino background for a high-pressure TPC using $^{82}\text{SeF}_6$. Previous studies show that, for ^{82}Se the single-beta decay events induced by the solar neutrino contribute 4.42 events/(ton·yr) in a 60 keV Region of Interest (ROI) window [20]. This value is large compared with that from the $2\nu\beta\beta$ process (0.15 events/(ton·yr)). This is because of the low interaction threshold ($Q_\nu = 172$ keV) for inverse beta decay of ^{82}Se to ^{82}Br . For TPC detectors, these backgrounds would have signatures that differ with respect to the signal and thus could be reduced using the tracking information. In this study, we use simulations to assess the signatures of various backgrounds and the rejection capability. A better understanding of these backgrounds would help the sensitivity estimation and design optimization of future projects.

The remainder of this paper is organized as follows. In Section II, we briefly describe the solar neutrino model and simulation setup of this study. We discuss each possible background source in Section III. Finally, we present our conclusions in Section IV.

II. SETUP

A. Solar neutrino flux

The neutrino flux data from the Standard Solar Model with low metallicity (B16-AGSS09, [21]) are used as a baseline. The energy spectra are shown in Fig. 2 (left). The differences between this model and other models [22,

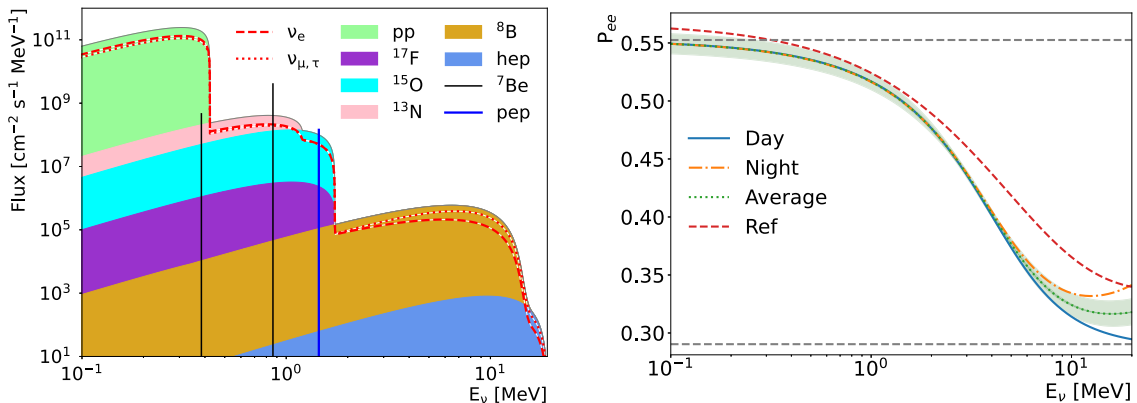


Fig. 2. (color online) Energy spectra of the solar neutrino (left) and electron neutrino survival probability as a function of its energy (right). The continuous energy spectra of various neutrino production processes are stacked. The neutrino from ^8Be and pep are drawn separately (in unit of $\text{cm}^{-2}\text{s}^{-1}$). The continuous spectra of ν_e and $\nu_{\mu,\tau}$ on Earth are also shown using P_{ee} in the right figure. In the P_{ee} distribution, the red dash curve shows the function used in [27]. The two horizontal dash lines show the P_{ee} without matter effect on top and two flavour mixing limit on bottom. The green band shows the uncertainty from the 1σ variation of the oscillation parameters.

[23] are quite small; the model dependence of our results will be discussed later. To calculate the survival probability, Eqn. (2.8) presented in [24] and the latest neutrino oscillation parameters from NuFit [25, 26] are used. The value $N_e = 100 N_A/\text{cm}^3$ is used to denote the electron density in the Sun, where N_A is the Avogadro constant. When considering the matter effect on Earth, the day-night difference is calculated using Eqn. (2.21) presented in [24]. As shown in Fig. 2(right), the values are generally smaller than those in [27]. Because the difference between day and night is small in the low energy region, the day-night average is used in this study. The resulting spectra of ν_e and $\nu_{\mu,\tau}$ on Earth are also shown in Fig. 2 (left).

B. Simulation

Signal and background processes are simulated using Geant4 (version 11.1.2) [28–30]. The Bearden data are used for determining the binding energies to obtain more accurate X-ray fluorescence lines. A detector with dimensions $40\text{ m} \times 40\text{ m} \times 40\text{ m}$ is built and filled with $^{82}\text{SeF}_6$ at 20°C temperature and 10 bar pressure. 100% enrichment of ^{82}Se is used for simplicity. Events are generated with their primary interaction points uniformly distributed in a $0.5\text{ m} \times 0.5\text{ m} \times 0.5\text{ m}$ cube around the center. Signal events are generated using the BxDecay0 package (version 1.1.0) [31]. For various neutrino background events, particle guns are used to emit electrons or ions. For the detection, we consider a hexagon grid readout plane with pitch size 8 mm as suggested in [9]. The maximum step size is set at 1 mm to obtain a fine segmentation of the tracks.

The simulation is divided into two parts. In the first part, the interactions of the final state particles of each process in the detector are simulated using Geant4. The steps that have non-zero energy deposition are recorded as "hits." In the second part, the energy of each step is converted to the number of electrons using the W -value, and assigned to pixels on the readout plane based on their location. As there is no measurement of the W -value for $^{82}\text{SeF}_6$ available, the value $W = 32\text{ eV}$ of the structurally similar SeF_6 gas is used to obtain the number of ion pairs. Based on the discussion presented in [8], a 0.34% FWHM smear of total energy is introduced to account for the Fano factor. To consider the diffusion of the track during the drift, the $x-y$ position of the ions are smeared using a Gaussian function having a 1 mm FWHM width. Existing studies and measurements suggest that this is achievable for a 1 m drift distance of ions by applying an electric field of approximately 65 kV/m [17, 32]. No smearing in the z direction is applied because the smear in the z direction also depends on the readout electronics, which has little impact to this study. In the second part, for efficient computing, the size of the detector is reduced to $7\text{ m} \times 7\text{ m}$ in the $x-y$ directions, a size that is already much

larger than that of any planned detectors.

In the event building, the signal in each pixel is divided into "blocks" based on the z profile of the signal. "Raw blocks" are built first based on the distance of the hits to their nearest neighbouring hits. If the distance is greater than 2 mm, they are added in two separate "raw blocks." The long "raw blocks" are divided into "blocks." If the length of a raw block in the z direction is greater than 8 mm, it is divided into several "blocks" with equal length, with the number of blocks being minimal. This division in the z direction, although having little impact on the results given in this paper, would facilitate other background studies to check the dE/dx for particle identification and use the Bragg peak feature to separate the signal and single-electron background, even if the track is along the z direction and contained in a single pixel. Adjacent blocks are further merged to form a "cluster." Regarding the energy of each block, a further smear corresponding to $40 e^-$ is applied to consider the uncertainty rising from recombination, readout electronics, and other effects. This yields an overall energy resolution of 1%.

Figure 3 shows the 3D "hits" of each step and 2D projection of the "blocks" after the reconstruction for one typical signal event. One can clearly see the larger energy depositions (Bragg peaks) at both ends of the track.

III. ANALYSIS

The neutrino could interact with the electrons or the ^{82}Se and ^{19}F nuclei. For electron-neutrino scattering (ES), the interaction is relatively simple, whereas for the interaction with nuclei, the subsequent decay of the nuclei in the final state could also mimic our signal and thus needs to be considered. Figure 4 illustrates the related interactions with the ^{82}Se and ^{19}F nuclei. ^{82}Se could be converted to the 1^+ excited state of ^{82}Br via a Charge Current (CC) interaction with the neutrino. The excited state of ^{82}Br decays to the isomer state ^{82m}Br ($J^\pi = 2^-$) via gamma radiation. Subsequently, ^{82m}Br could decay to the ground state by radiating a 46 keV gamma with a 97.6% branching fraction or proceed with a β^- decay to ^{82}Kr directly with a 2.4% branching fraction. ^{82m}Br has a large probability (88%) to decay to the ground state of ^{82}Kr . In contrast, the decay of ground state ^{82}Br to the ground state of ^{82}Kr is forbidden. Thus, it decays to the excited states of ^{82}Kr , which subsequently decays to the ground state of ^{82}Kr , radiating multiple gammas. The picture for ^{19}F is simple, as in the CC interaction it would transit to the ground state of ^{19}Ne , which in turn decays back to ^{19}F via β^+ decay. Two 0.511 MeV gammas are produced from the positron-electron annihilation.

Figure 5 shows the energy spread (the largest distance between the interaction point and the location of any energy deposition, L) and number of reconstructed clusters in these processes. Signal events typically have a

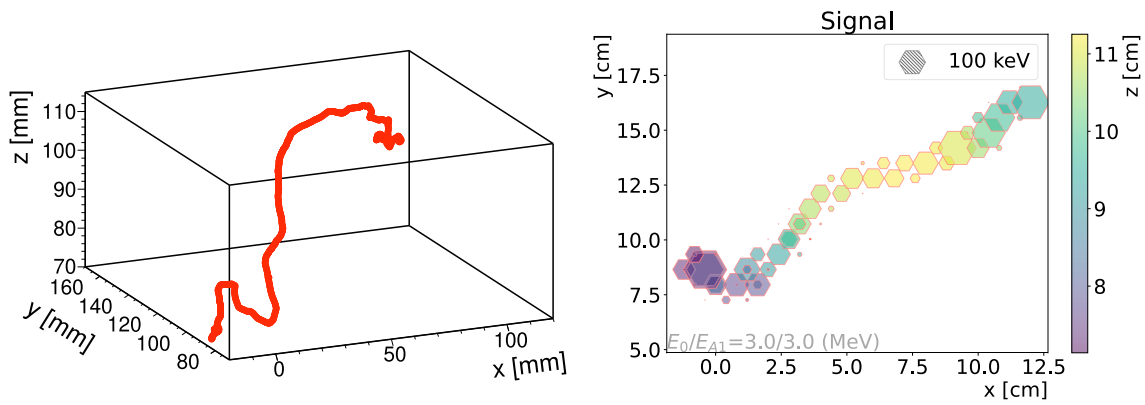


Fig. 3. (color online) 3D "hits" obtained in the Geant4 simulation (left) and 2D projection of the "blocks" after the reconstruction (right) for a signal event. In the 2D view, the energy deposited in each pixel is represented by the size of the hexagon. The size corresponding to 100 keV energy is shown in the legend. The z coordinate is represented by the color of the filled hexagon. The blocks with the same edge color belongs to the same cluster. For the leading and sub-leading clusters, red and blue are used for the edges. The text in the bottom left corner gives the energy of the leading cluster (E_0) and total energy (E_{AN} , where N is the number of clusters in the event). In this event, all blocks are collected in a single cluster.

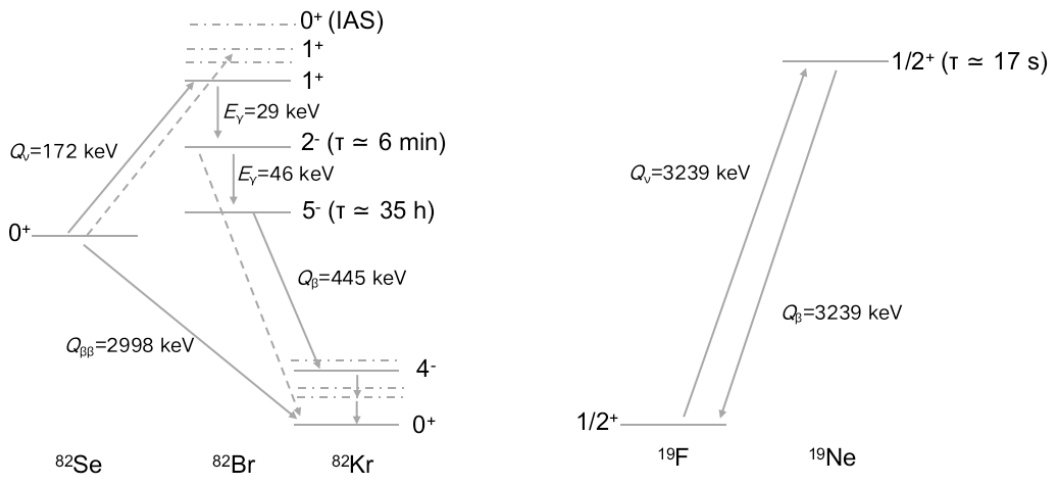


Fig. 4. Schematics of the interactions for ^{82}Se (left) and ^{19}F (right). The most relevant levels and transitions are shown as solid lines. The less relevant levels are shown as dash-dot lines, and the transitions having small contributions are shown as dash lines.

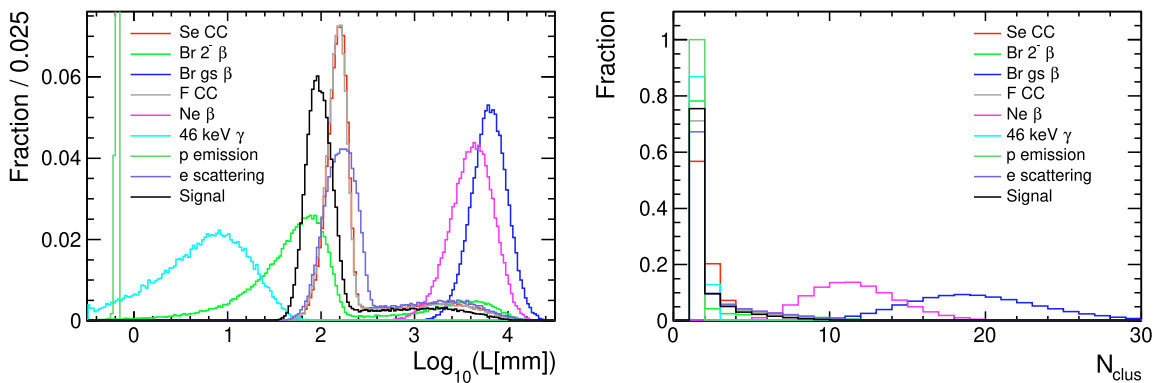


Fig. 5. (color online) Furtherest energy deposition from the interaction point (left) and the number of reconstructed clusters (right) for various processes.

spread $L \sim 10$ cm, but there is a long tail on the large L side due to bremsstrahlung gammas. The ^{82}Br (g.s.) and ^{19}Ne decays have a much larger energy spread and more clusters than other processes because of the production of high energy gammas. The distribution of the energy of the reconstructed clusters for each process is shown in Fig. 6. As expected, the signal events peak at $Q_{\beta\beta}$ region, but there also exists a significant fraction of events having low energy clusters. They are again mainly due to the bremsstrahlung gammas. The various background processes are discussed in detail in the following subsections.

A. Electron scattering

All three flavors of neutrinos could exhibit neutral current (NC) interactions with electrons; in addition, for electron neutrino, CC interaction could also happen. These processes are widely utilized in the solar neutrino studies [33–36]. As possible backgrounds for neutrinoless double beta decay search, they have been studied for Ge [37] and other isotopes [38]. The differential cross-section for a neutrino with energy E_ν is [39, 40]

$$\frac{d\sigma}{dT} = \frac{2G_F^2 m_e}{\pi} \left[g_L^2 + g_R^2 \left(1 - \frac{T}{E_\nu}\right)^2 - g_L g_R \frac{m_e T}{E_\nu^2} \right], \quad (1)$$

where T is the kinetic energy of the outgoing electron, G_F is the Fermi constant, $g_L = \sin^2 \theta_W \pm \frac{1}{2}$ (the upper sign is for ν_e and lower sign for ν_μ and ν_τ) and $g_R = \sin^2 \theta_W$ are the coupling parameters, and θ_W is the Weinberg angle. The maximum value that T could reach is $T_{\max} = \frac{2E_\nu^2}{m_e + 2E_\nu}$. The angle between the electron and neutrino

momenta, θ , is given by

$$\cos^2 \theta = \frac{T(m_e + E_\nu)^2}{(T + 2m_e)E_\nu^2}. \quad (2)$$

For simplicity, the radiative correction leading up to a 4% reduction [41] of the cross-section is not included, as the effect is much smaller than the uncertainty arising from the neutrino flux.

Figure 7 (left) shows the energy spectrum of electron. The contribution from $\nu_{\mu,\tau}$ is approximately 0.22, including the effect from oscillation and the difference in cross-sections. The total event rate is 481.0 events/(ton-yr); however, the vast majority of the recoil electrons have a low energy from the pp neutrinos. The event rate drops by four orders of magnitude between the pp neutrino region and ROI at approximately 3 MeV. The estimate is 0.00445 events/(30 keV ton-yr) near the ROI, with a relative uncertainty of 12% from the neutrino flux, consistent with the results obtained by scaling the numbers presented in [38].

The signatures of this type of events are the same as those of the single electron events occurring due to natural radioactive decays. 100k ES events with $2 < T < 5$ MeV are simulated. Observe from Fig. 5(left) that the distribution of the spread is similar to signal events, but the mean is larger. The wider distribution is due to the large energy range. Moreover, these events have a small number of clusters. A typical event is shown in Fig. 7 (right). The algorithms developed to distinguish the radioactive decay background could also be used to reject this background. Machine learning methods show promising results in this domain [7, 8, 42, 43].

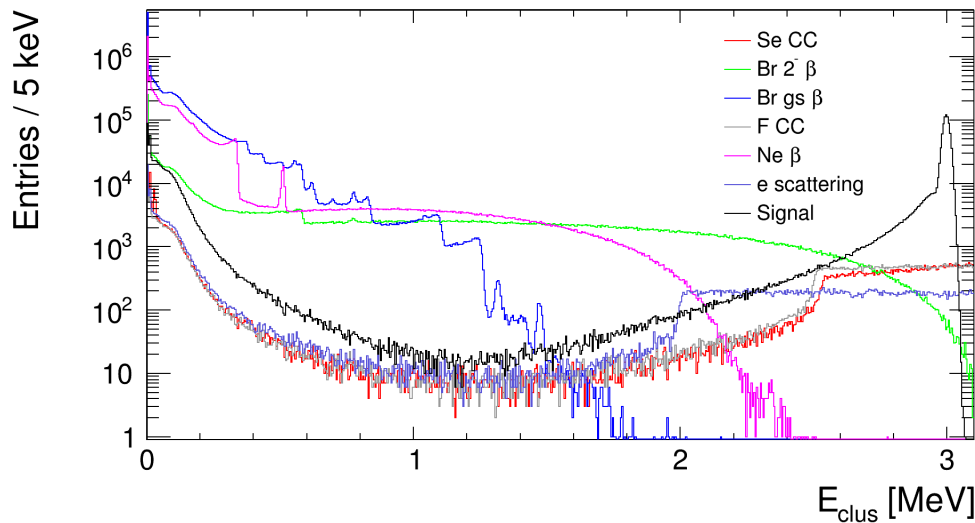


Fig. 6. (color online) Distribution of the energy of the clusters. For Se CC, F CC, and ES processes, only the events that are in the energy window are simulated. Thus, the step structure occurs at 2 MeV for ES and approximately 2.5 MeV for Se CC and F CC. For other processes, the full spectra are used. 1M events are generated for Br decay, Ne decay, and signal events, and 100k events are generated for other processes.

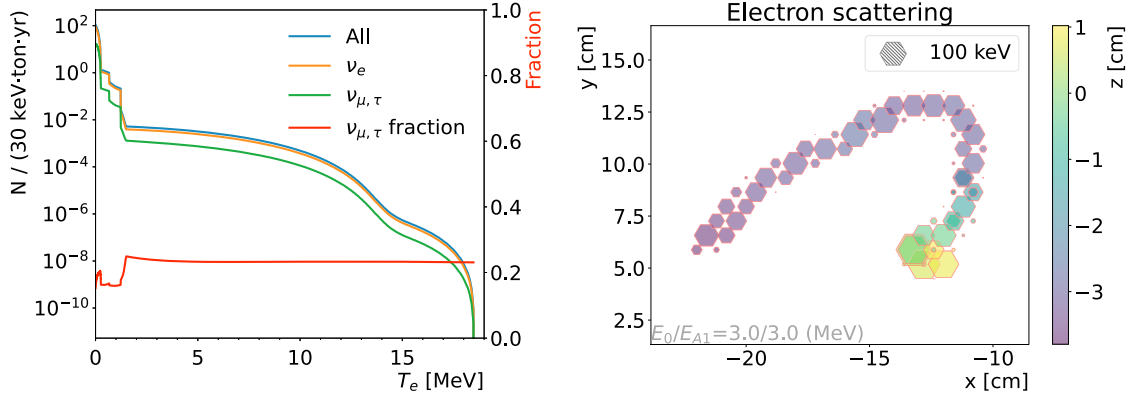


Fig. 7. (color online) Energy spectra of the outgoing electron (left) and the event display of one typical ES event (right).

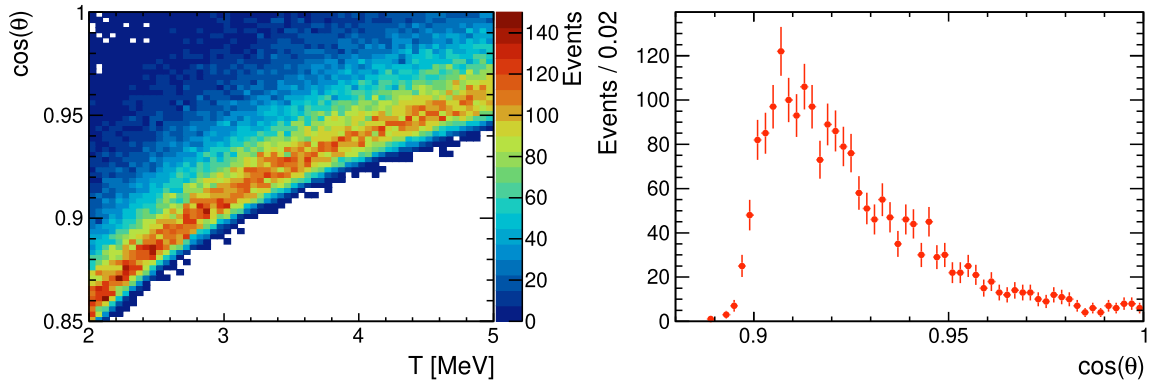


Fig. 8. (color online) $\cos\theta - T$ distribution for electrons in the range $2 < T < 5$ MeV (left). The distribution of $\cos\theta$ for electron scattering events with $|T - Q_{\beta\beta}| < 30$ keV (right).

As there is a strong correlation between the neutrino momentum direction and outgoing electron momentum direction, the angular information might also help the signal/background classification. Figure 8 plots the cosine value of the zenith angle. It peaks at $\cos\theta \sim 0.9$, corresponding to $\theta \sim 25^\circ$, which is expected because the majority of the electrons are from the interaction of the ^8B neutrino that peaks at approximately 6 MeV in the energy distribution. Track direction determination similar to that implemented in [44] could be used to extract the angle. While a selection based on the angles would always bring inefficiency for signal classification, alternatively, the angular variables could be added in the machine learning methods to provide extra information.

B. Nuclei CC processes

As transition to the ground state of ^{82}Br is forbidden, when interacting with the solar neutrino, the ^{82}Se could undergo an inverse beta decay to the excited states of ^{82}Br ,

$$\nu_e + ^{82}\text{Se} \rightarrow e^- + ^{82}\text{Br}^*, \quad (3)$$

and $^{82}\text{Br}^*$ will mainly remain in the 1^+ Gamow-Teller

(GT) states. The lowest of such a state is the 75 keV excitation energy state. The threshold of this process is $Q_\nu = 172$ keV. The final state electron will have energy $E = E_\nu - Q_\nu$. Transition to the 0^+ Isobaric Analog State (IAS) is also possible for high energy neutrinos, but it is suppressed by the low neutrino flux due to the high threshold $Q_\nu = 9.673$ MeV.

The cross-section for the transition to the excited state k is [45]

$$\begin{aligned} \sigma_k &= \frac{G_F^2 \cos^2 \theta_c}{\pi} p_e E_e F(Z, E_e) \left[B(F)_k + \left(\frac{g_A}{g_V} \right)^2 B(GT)_k \right] \\ &= (1.597 \times 10^{-44} \text{ cm}^2) p_e E_e F(Z, E_e) \\ &\quad \times \left[B(F)_k + \left(\frac{g_A}{g_V} \right)^2 B(GT)_k \right], \end{aligned} \quad (4)$$

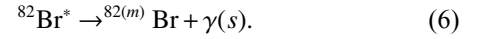
where θ_c is the Cabibo angle, p_e (E_e) is the outgoing electron momentum (total energy), and $F(Z, E_e)$ is the Fermi function. In this section, only the transition to the GT states is considered, leaving the discussion of IAS to Section III.E. For these GT states, the Fermi response $B(F) = 0$, and the values of Gamow-Teller response, $B(GT)$, for each GT states are taken from [14], following

the same configuration: individual resonances are used for $E_k < 2.5$ MeV, and the values in each bin are used for $E_k \geq 2.5$. The calculated yield is consistent with the values reported in [14] and [20]. In this calculation, the Fermi Function takes the form

$$F(Z, E_e) = L_0 F_0(Z, E_e), \quad (5)$$

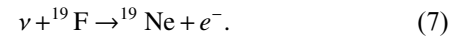
where $F_0(Z, E_e)$ is the conventional point charge Fermi Function, and L_0 is the correction factor for a finite-sized nucleus [46]. It is determined that the influence of the Fermi Function could be as large as 15% for ^{127}I [47]. The impact to our process is still to be assessed; however, the uncertainty arising from $B(GT)$ and the solar neutrino flux is already $\sim 12\%$ [14]. The total event rate is calculated to be 64.0 events/(ton·yr) without the oscillation effects. The dominant contribution is from the 75 keV state, as the higher states have a lower neutrino flux and smaller $B(GT)$ values usually. The event rate is larger than that of many other potential neutrinoless double beta decay isotopes due to the low threshold [48]. Including the oscillation effects, the yield decreases to 33.9 events/(ton·yr). The energy spectrum of the electron is shown in Fig. 9. Only 0.00021 events/(ton·yr) are within the ROI.

The excited states will decay to the isomer state ^{82m}Br , the excitation energy of which is 46 keV. ^{82m}Br has a half-life of $T_{1/2} = 6.13$ min, decaying either to the ground state of ^{82}Se by radiating a 46 keV gamma or to the ground state of ^{82}Kr via a β decay. The ground state, with $T_{1/2} = 35.28$ h, decays to excited states of ^{82}Kr via a β decay. Therefore, a long enough time interval exists to separate the CC process and the decay of ^{82}Br and ^{82m}Br . During the deexcitation, the following gamma radiation occurs:



Accordingly, the 75 keV state would release a 29 keV gamma and decay to ^{82m}Br . Therefore, in the detector, we would simultaneously observe an electron from the CC process and a 29 keV gamma. As the energy of the gamma is low and the transitions have large Internal Conversion (IC) coefficients, it loses its energy not far from the electron track. When IC happens, the characteristic X-rays might also be reconstructed. Note that the energy of the X-rays for Se and Br are slightly different: $E_{K_\alpha} = 11.2$ keV for Se and $E_{K_\alpha} = 11.9$ keV for Br. In principle, one might be able to identify the production of ^{82}Br from its characteristic E_{K_α} if the detector resolution is good enough. However, it is extremely challenging as the energies are very close; an energy resolution better than 6% RMS would be needed. As the half-life of ^{82m}Br is just 6.13 min and it has a 97.4% chance to decay to the ground state while releasing a 46 keV gamma, the coincidence of a 46 keV gamma at the same location could be used to identify the process and reject it. The IC coefficient is huge for this M3 transition. Approximately 12.9% of the 46 keV gamma radiation results in two clusters: one from the K_α X-ray and the other one from the IC electrons. The spread of this low energy gamma is at the cm level, as shown in Fig. 5 (left).

For ^{19}F , the process is very similar and much simpler. The transition can go the ground state of ^{19}Ne directly, but the threshold is much higher $Q_\beta = 3.24$ MeV. Therefore, in the final state, there is only a single electron:



^{19}Ne has a half-life of 17.22 s. Because the diffusion of the ion in 17.22 s spans only approximately a couple of

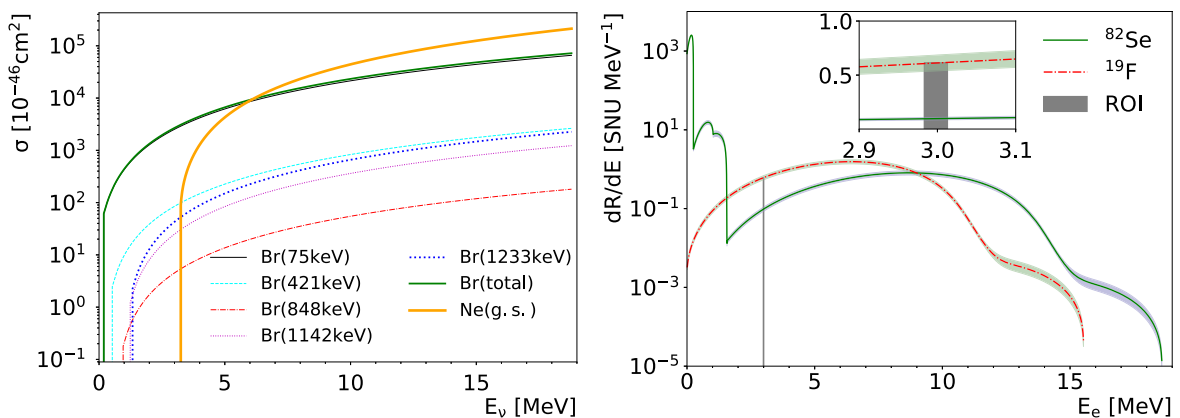


Fig. 9. (color online) Interaction cross-section for ^{82}Se and ^{19}F as a function of the neutrino energy (left) and capture rates as a function of the electron energy for ^{82}Se and ^{19}F (right). In the capture rate distribution, only the continuum is shown. The discrete contributions from ^{10}Be and pep to the ^{82}Se case that are far below the ROI are not shown. The uncertainty bands are from the neutrino flux data only. The capture rates near the ROI are shown in the inset.

centimeters, the coincidence of a CC electron and the β^- decay at the same location within tens of seconds could be used to identify this process.

The cross-section can be calculated using Eqn. (4) with $B(GT) = 1.61$ and $B(F) = 1$ from [15]. The differential cross section and capture rate are also shown in Fig. 9. The total capture rate is 8.8 (2.9) SNU (solar neutrino unit, $= 1 \times 10^{-36}$ interactions per target atom per second) without (with) the oscillation effect, and it corresponds to an event rate of 5.1 (1.7) events/(ton·yr).

For each CC process, 100k events are simulated within the electron energy in the range of 2.5 to 3.5 MeV. Figure 10 shows the example events of the CC process for ^{82}Se and ^{19}F . Observe from Fig. 5 that the spread and cluster multiplicity are consistent with the single electron events. Note that, in the Br CC process, we have only simulated the 75 keV state, which accounts for 97% of the total capture rate as shown in Fig. 9. If ^{82}Br is excited to higher states, high energy gammas will also be produced. For example, the next major contributing state, the 421 keV state, will decay to the 75 keV state and radiate a gamma with an energy 345 keV. The gamma radiation will increase the spread and number of clusters. Because the signatures of the decays of ^{82}Br and ^{19}Ne are quite different, they are discussed separately in the next two subsections.

C. Decay of ^{82}Br

In the beta decays of ^{82}Br and ^{82m}Br ,



an electron will be produced, accompanied with gammas if they decay to the excited states of ^{82}Kr . ^{82}Br (g.s.) has $\sim 96.9\%$ chance to decay to the 2.648 MeV excited state of ^{82}Kr . As shown in Fig. 6, multiple photoelectron peaks and the Compton edges from the ^{82}Br decay process can be clearly observed in the reconstructed clusters. As part of the energy will be taken by the neutrino, the majority of the events have a total energy deposition in the detector or less than the maximum $Q = 3.093$ MeV. Moreover, ^{82m}Br dominantly ($\sim 88.1\%$) decays to the ground state of ^{82}Kr , with a small fraction to other excited states: 9.2% to the 777 keV state, 2.1% to the 1475 keV state, and $<0.3\%$ to others. Among them, only the Compton edge for the 777 keV state is visible. The Q value for ^{82m}Br is also slightly higher at $Q = 3.14$ MeV. The spectra of the total energy for both decays are shown in Fig. 11, calculated using BetaShape [49]. Approximately 1.9% of the ^{82}Br (g.s.) decay has a total energy within the 30 keV window around $Q_{\beta\beta}$. For ^{82m}Br , only 0.0015% is in the ROI window (the 2.4% branching fraction for direct β^- decay is included). The ^{82}Br decay will be a multi-site event due to the multiple gammas; thus, this feature could be used for background rejection. ^{82m}Br decays to the 777 keV state in a similar manner; however, for ^{82m}Br decay to ^{82}Kr (g.s.), there is only a single electron, and one needs to leverage the Bragg peaks to distinguish it.

Considering that ^{82}Br predominately decays to the 2.648 MeV state of ^{82}Kr and the electron from the beta decay usually forms only one cluster, we can calculate the "N-1" cluster energy for cluster i as follows: $E_{N-1,i} = E_{\text{tot}} - E_i$, where $E_{\text{tot}} = \sum_j E_j$ is the total energy of the event. When the cluster formed by the electron is removed, $E_{N-1} = 2.648$ MeV is the excitation energy of ^{82}Kr ; for other clusters, it would be random. Therefore, all these events would have at least one cluster having E_{N-1} close to 2.648 MeV. Fig. 12 shows the distribution of E_{N-1} for all clusters. The peak at 2.648 MeV can be clearly seen on top of the continuum from random remov-

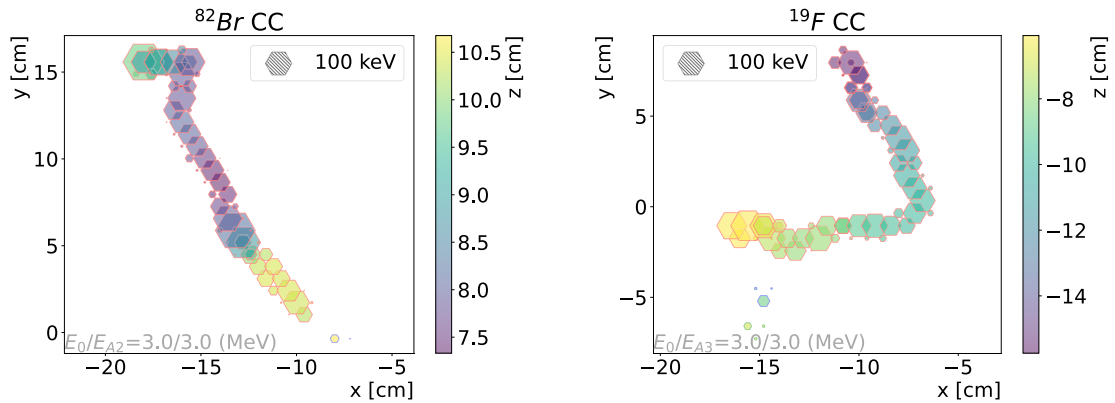


Fig. 10. (color online) Event display for ^{82}Se CC (left) and ^{19}F CC (right) processes. There are two clusters built in the ^{82}Se CC event. The small cluster containing only two pixels in the bottom right corner, with the blue edge, is from the 11 keV K_α X-ray of ^{82}Br . The two small clusters in the ^{19}F event are due to the bremsstrahlung gamma.

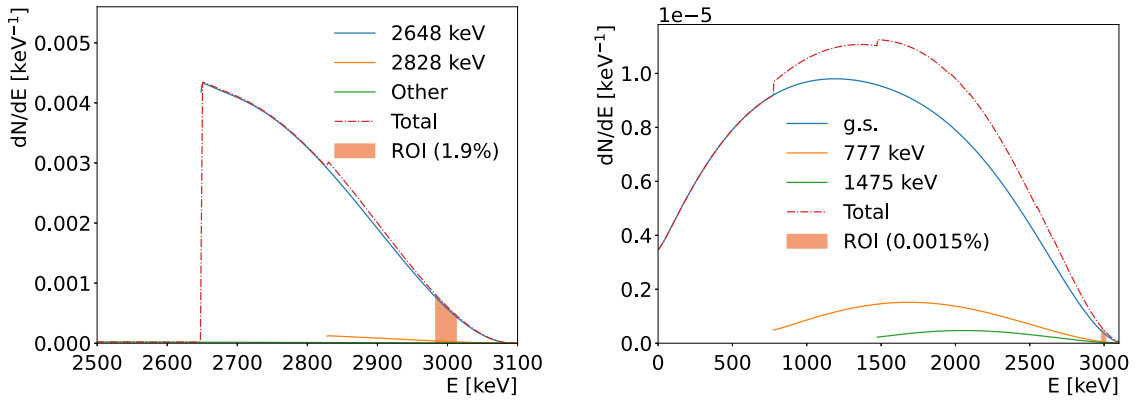


Fig. 11. (color online) Distribution of the detectable energy in ^{82}Br (g.s.) decay (left) and ^{82m}Br decay (right). The red dash curves show the total energy, while the breakdown of the main processes to various excited states of ^{82}Kr are shown by solid curves. Filled areas show the ROI with the 30 keV mass window centered at $Q_{\beta\beta}$. The left figure is normalized to unit, and the right one is normalized to the branching fraction of ^{82m}Br beta decay, 2.4%.

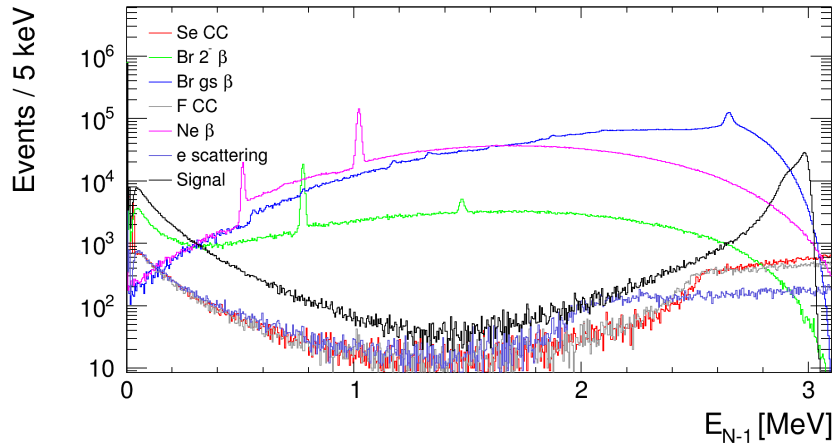


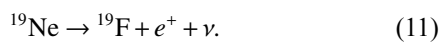
Fig. 12. (color online) Distribution of E_{N-1} in various processes.

al. For the ^{82m}Br decay, the 777 keV and 1475 keV peaks are also clearly visible.

One needs to be careful here since, in some $0\nu\beta\beta$ models, ^{82}Se could decay to the excited states of ^{82}Kr , namely the 777 keV 2^+ state and 1488 keV 0^+ state. In that case, the 777 keV gamma and a 711 keV gamma could also appear in the final state of $0\nu\beta\beta$ signal events. The $2\nu\beta\beta$ decay to these states are not experimentally observed yet [50].

D. Decay of ^{19}Ne

^{19}Ne has a short half-life of 17.22 s; thus, it will decay back to ^{19}F soon after it is produced through a β^+ decay:



The maximal detectable energy is $Q = 3.24$ MeV. The spectra of the total detectable energy are shown in Fig. 13(left). Approximately 0.25% of the events are in the 30

keV wide ROI.

In the detector, the energy deposition comes from a positron track starting at the decay point and two gammas from the electron-positron annihilation at the end point of the positron track. As shown in Fig. 6, the Compton electrons and photoelectrons are reconstructed as clusters. Figure 13 (right) shows a typical event. The energetic gamma could yield multiple Compton scatterings in the detector, resulting in a wide spread of energy and multiple clusters. The number of clusters could be used to reject these background events. By imposing $N_{\text{cluster}} < 5$, approximately 99.6% of the events are removed. To identify the events, we can use E_{N-1} to reconstruct the annihilation peak. Observe from Fig. 12 that the peak occurs at approximately 1.022 MeV. Another prominent peak shows up at $E = 0.511$ MeV, corresponding to the events in which one gamma has escaped the detector. These features could also be used to veto the ^{19}F CC process using the time coincidence as already mentioned in Section III.B.

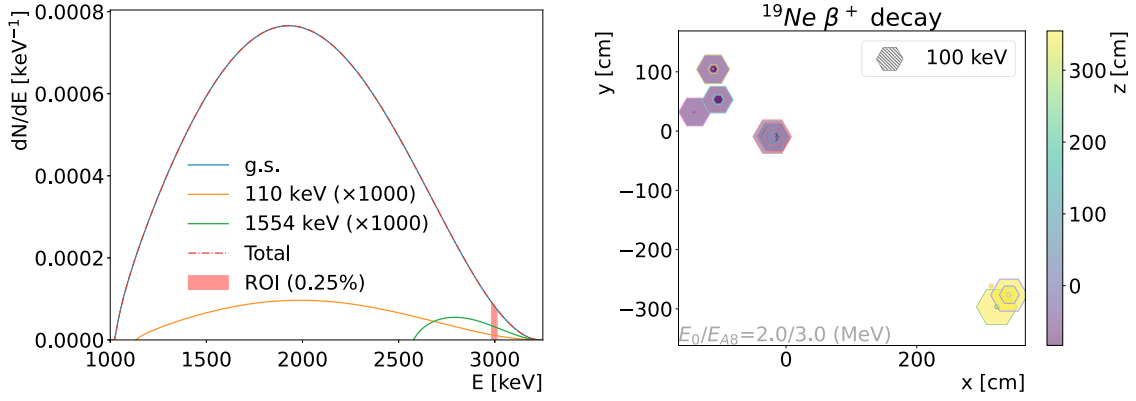


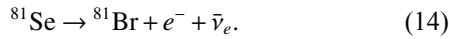
Fig. 13. (color online) Distribution of the detectable energy in ^{19}Ne decay (left) and the display of one typical event (right). The contributions from the 110 keV state and 1554 keV state are approximately four orders of magnitude smaller than that of the ground state; thus, they are multiplied by a factor of 1000 to make them visible.

E. Particle emission

If E_ν is higher than the threshold for particle emission ($S_n = 7.593$ MeV and $S_p = 8.399$ MeV), ^{82}Br could reach the broad Gamow-Teller resonance (excitation energy $E_x \approx 12.1$ MeV and width of ≈ 5 MeV) or IAS (excitation energy 9.576 MeV), decay via emitting a proton (neutron), and transit to ^{81}Se (^{81}Br):



^{81}Se decays to ^{81}Br through a β decay, with $Q_\beta = 1588$ keV:



The long lifetime of $T_{1/2} = 18.45$ min makes it less signal-like, facilitating the separation of production and decay. Using Eqn. (4) and setting $B(F) = 13.8$ [14], the event rate for IAS production is calculated to be 0.093 events/(ton·yr).

For neutron emission, the signature differs significantly with signal. Therefore, here, we only discuss the proton emission briefly. The energy of the proton from IAS decay is 1.18 MeV. This energy is significantly below our signal ROI, and because the proton is much heavier than the electron, the proton track is much shorter than the electron tracks, as shown in Fig. 5. Considering the low production rate, we conclude that this background could be safely ignored.

F. Other isotopes

For Fluorine, ^{19}F is predominant; thus, the contribution from other isotopes is negligible. If ^{82}Se is not enriched to 100%, we also need to consider the CC interac-

Table 1. Information of the Se isotopes and corresponding Br isotopes.

Isotope	Abundance(%)	Q_β /MeV	$Q_{\beta\beta}$ /MeV	Br lifetime	Br decay
^{74}Se	0.86	6.925	1.209	25.4 min	β^+
^{76}Se	9.23	4.963	—	16.2 h	β^+
^{77}Se	7.6	1.365	—	57 h	β^+
^{78}Se	23.7	3.574	—	6.45 min	β^-, β^+
^{80}Se	49.8	1.870	0.134	17 min	β^-, β^+
^{82}Se	8.82	0.095	2.998	35 h	β^-

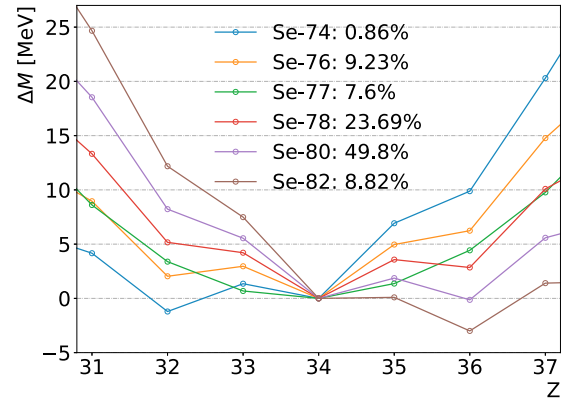


Fig. 14. (color online) The mass difference $\Delta M = m_X - m_{\text{Se}}$ for isotope X with the same A . Only the Se isotopes that have known non-zero abundance values and isotopes that have the same A are shown. The numbers in the legend give the exact abundance of each Se isotope.

tion and subsequent decays of other isotopes. The isotopes with known abundance are listed in Table 1, and their mass differences with the nearby isotopes are shown in Fig. 14.

For the CC process, these isotopes all have higher thresholds and thus smaller capture rates. Moreover, we have shown that, even for the ^{82}Se CC process, the direct

background from CC is small because only a small fraction of the outgoing electrons have their energy in the small ROI window. ^{74}Br , ^{76}Br , and ^{77}Br go through a β^+ decay back to Se. The annihilation peak discussed in Sect. III.D could be used for identification. For ^{78}Br and ^{80}Br , in addition to the β^+ decay to Se, they could go to Kr via β^- decays; however, the released energy is quite small. They may also proceed with an Electron Capture (EC) process, in which case, the visible energy deposit from the X-rays is even smaller. The Br isotopes all have a relatively long lifetime (Table 1). Therefore, the production and decay could be well separated in the detection.

G. Discussion

The background could be divided into two categories: 1) single-electron background, i.e., a background that has a single electron in the final state, with or without a low energy gamma, and 2) multi-site background, i.e., a background that has one or more energetic gammas in the final state. The immediate results of the CC process belongs to the first category. Although, in the ^{82}Br CC process, a 29 keV gamma is observed, its energy is too low to be well separated from the electron track. The β decay of ^{82m}Br is also in this category. The decays of $^{82}\text{Br}(\text{g.s.})$ and ^{19}Ne belong to the second category.

For the single-electron background, the main feature that can be used to separate the signal and background is the two Bragg peaks in signal events in contrast to the single Bragg peak in background events. The two Bragg peaks can be clearly seen in the example signal events shown in Fig. 3. There are numerous studies regarding this type of background, and a background suppression factor of 10 or more could be achieved while keeping a high signal efficiency [7, 8, 10, 42]. Therefore, here, we focus on the multi-site background. As there are gammas in these final states, they usually form multiple clusters,

and the detection of individual gammas becomes possible. As shown in Fig. 6, the photoelectron peaks and Compton edges can be clearly seen. The peaks are useful to tag the process. For ^{19}Ne decay, we could also see the gamma from annihilation and its Compton edge. In these events, the electron or positron from the β^\pm decay usually forms a cluster, which often corresponds to the cluster with the highest energy. Figure 15 shows the energy of the leading cluster. As expected, in the signal events, the leading cluster has an energy level close to $Q_{\beta\beta}$. However, for ^{82}Br decay, the highest energy cluster is from the 1475 keV gamma. When ^{82}Br decays to the 777 keV excited state, the energy of the electron from this decay could be up to 2.31 MeV; however, the corresponding branching fraction is very small (0.7%). For ^{19}Ne decay, the energy of the positron stops at approximately $3.24 - 1.022 = 2.2\text{MeV}$. Thus, a simple cut requiring the energy of the leading cluster to be $E_0 > 2.2$ MeV could remove these events. In the simulation samples containing 1M events, the ^{82}Br decay has 0 events left, while the ^{19}Ne decay has 19 events. An upper limit of the ^{82}Br decay background event rate of < 0.0001 events/(ton·yr) could be set at a 95% C.L. By further requiring $N_{\text{clus}} < 5$, the number of ^{19}Ne decay events is reduced to 2, corresponding to an event rate of 0.000003(3) events/(ton·yr). The signal efficiency is 98% after the $E_0 > 2.2$ MeV cut and 93% after the $N_{\text{clus}} < 5$ cut.

So far, we have assumed a rather large detector, where almost all the energy of the electrons, positrons, and gammas are collected. In this way, we avoid entangling the physical interactions inside the detector and the boundary effects. In a real detector, there are various boundary effects. For example, the interactions that happen close to the boundaries will result in only part of the energy being deposited inside the fiducial region. The fraction of such events depends on the size and geometry of the detector. When considering the boundary effects,

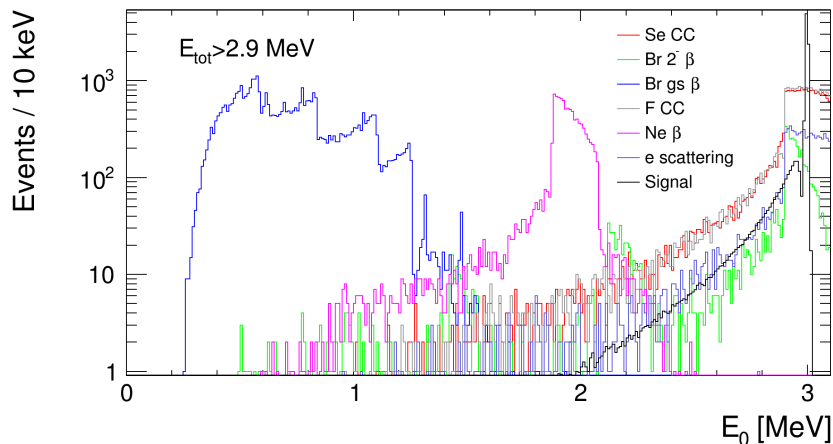


Fig. 15. (color online) Distribution of the energy of the leading cluster. The distribution of signal events is scaled by 0.01 to fit the range of other processes.

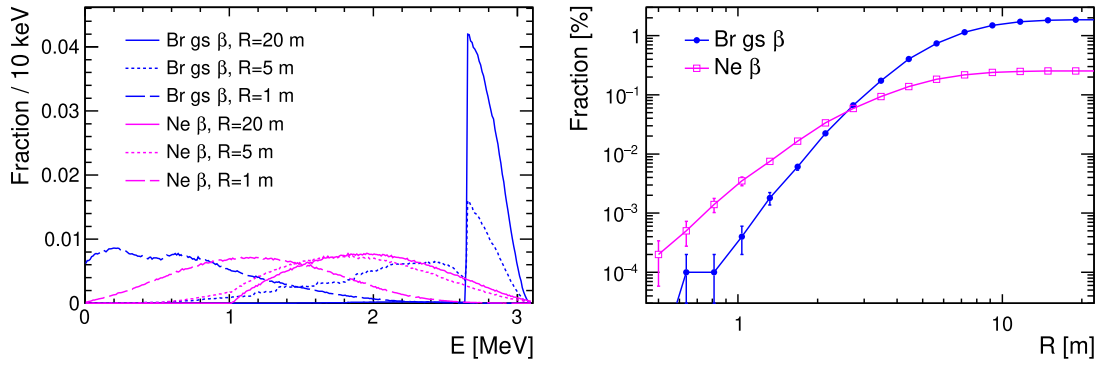


Fig. 16. (color online) Distributions of the detectable energy within radius $R = 1$ m, 5 m, and 20 m from the interaction point (left) and the fraction of events in the ROI as function of R (right) for multi-site background processes.

the rejection power of the cut $N_{\text{clus}} < 5$ might degrade because the multi-site background events will have a smaller number of clusters built inside the detector. However, this degradation will be compensated by the reduction of the event rate in the ROI. Figure 16 shows the effect of the detector size on the distribution of the detectable energy and event rate in the ROI. For small detectors, the distribution of the detectable energy shifts to the lower side, with a smaller number of events in the ROI. Notice that the fraction of events in the ROI decreases rapidly as the detector size becomes less than a few meters. This trend is consistent with the energy spread distributions depicted in Fig. 5 (left). Contrarily, the detector size should not affect the E_0 cut, which remains effective until the detector size becomes smaller than the size of signal events. For a real detector, one would need to optimize the selection cuts based on its size and geometry. The results we obtain here suggest that, using the abovementioned features, one could suppress the multi-site backgrounds with some simple cuts while maintaining a high efficiency for the signal.

Table 2 presents a summary of the backgrounds. We can effectively reduce the background using the tracking information while maintaining a high efficiency for signal events. Assuming a reduction factor of 10 for the single-electron background, the total background in the 30 keV ROI window should be below 0.001 events/(ton·yr).

The major contributors of the ^{82}Br β decay backgrounds are pp and ^7Be neutrinos because of their high fluxes. For ES, ^{82}Se CC, ^{19}F CC, and ^{19}Ne β decay backgrounds, due to the requirement of high E_ν , the contribution from ^8B dominates. The high metallicity models predict higher ^7Be and ^8B neutrino fluxes; thus, more background events are expected. The increases are approximately 3% for ^{82}Br β decay and 20%–30% for other processes. Figure 17 shows a comparison of the total capture rate obtained from various flux data. Note that Fig. 17 (right) for ^{19}F also applies to other backgrounds that require high E_ν in the ^8B neutrino range.

Table 2. Summary of the background in unit of events/(ton·yr). The numbers with * marks in the last column could be further reduced using the energy distribution information in the cluster. The 95% C.L. limits are calculated from the upper limit of the yield 3 events for zero observed events. The last column lists the expected number of events after the selection cuts $E_0 > 2.2$ MeV and $N_{\text{clus}} < 5$. The uncertainties given in the parentheses are statistical only.

Source	All energy	With oscillation	ROI	Selection
Electron scattering	728.6	481.0	0.00445	0.00395(13)*
^{82}Se CC	63.95	33.88	0.00021	0.000185(4)*
^{82}Br β decay	62.41	33.07	0.63	< 0.0001 (95% C.L.)
^{82m}Br β decay	1.54	0.81	0.00052	0.00037(2)*
^{19}F CC	5.11	1.69	0.0036	0.00318(7)*
^{19}Ne β decay			0.0042	0.000003(3)
Proton emission	0.292	0.093	0	0
Total single-electron events			0.00878	0.00769(15)
Total multi-site events			0.63	< 0.0001 (95% C.L.)

We have shown that several unique features of the background process are useful for background rejection. The successful identification could also be used for solar neutrino studies. With good energy resolution and tracking capability, using a single cluster, we can already observe various characteristic gamma peaks (Fig. 6). Using E_{N-1} , we can also obtain the information of the excited states (Fig. 12). A more sophisticated combination of the clusters might increase the efficiency of the tagging. The directional information of the electron scattering would also be useful. As ^{19}F and ^{82m}Br have a short half-life, the coincidence of the time and location could also be used. The feasibility of using this information in solar neutrino experiments should be further studied.

Lastly, current results are obtained with some assumptions that are yet to be confirmed experimentally.

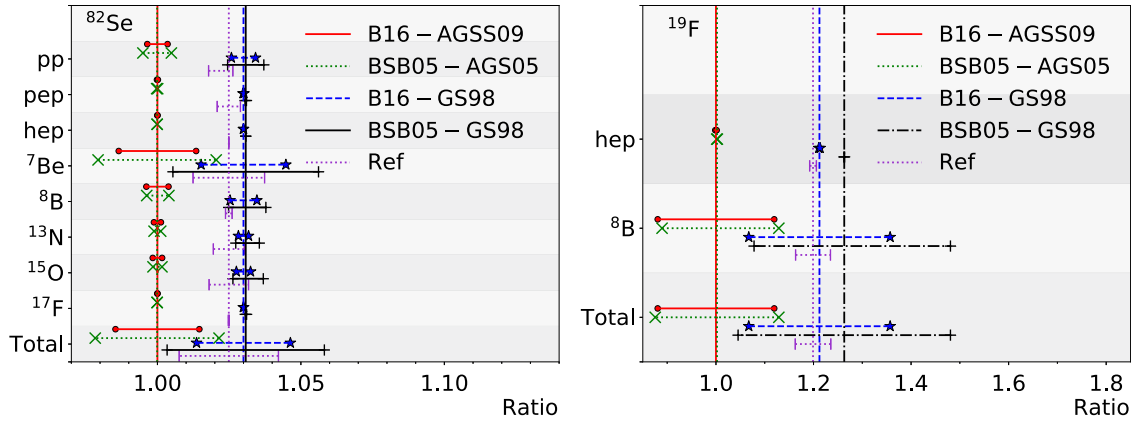


Fig. 17. (color online) Ratios of the predicted capture rates from various solar neutrino flux data to the baseline (B16-AGSS09 model) for ^{82}Se (left) and ^{19}F (right). The total captures are shown at the bottom, and the relevant breakdowns are shown above them. Horizontal bars are obtained by varying the flux by the 1σ uncertainty given by the model. The flux data are taken from Table 2.1 of [24] and Table III of [14].

First, we have assumed a good energy resolution (1% FWHM) that allows us to use a small ROI window. The identification of background processes using the characteristic gamma peaks also demands excellent energy resolution (Figs. 6 and 12). The energy resolution roughly depends on two factors: the number of pixels used to collect the energy of an event and the electrical noise of the pixels. In this study, we have assumed a total noise of 40 e^- for each readout channel. Recent development shows that this level of low-noise is achievable [9, 51]; however, a readily usable chip does not exist. The number of pixels hit by one event depends on the pitch size and diffusion. The low diffusion of ion drift is confirmed in various measurements [17, 32], but no measurements of ions in $^{82}\text{SeF}_6$ have been conducted so far. The choice of an 8 mm pitch size in this study is based on the results reported in [9], which should be revisited once we have better knowledge about the diffusion and the electrical noise of the readout chip. Second, the cuts we have used, namely the energy of the leading cluster and the number of clusters, require good tracking capability to separate energy clusters. This also depends on the pitch size and diffusion. Finally, if the TPC operates at a different pressure, the pitch size might need to be adjusted to maintain

the same performance level.

IV. CONCLUSIONS

Background from solar neutrino is potentially important for neutrinoless double beta decay experiments. Here, the detector response of a high-pressure $^{82}\text{SeF}_6$ gaseous TPC to solar neutrino events is studied via simulations. We found that the background could be effectively rejected using the cluster information, taking advantage of the good energy and spatial resolution of the TPC. By simply setting the energy of the leading cluster as $E_0 > 2.2$ MeV and number of clusters as $E_{\text{clus}} < 5$, we can reduce the expected number of background to < 0.001 events/(ton·yr) in a 30 keV ROI window around $Q_{\beta\beta} = 2.998$ MeV. This is sufficient for a ton-yr level exposure. For a larger exposure, further optimization using the real detector setup could be conducted in a similar manner. Given the rich features of the background, it is anticipated that a large detector, equipped with good energy and spatial resolution, would be capable of effectively harnessing these characteristics to achieve an appropriate level of background control. These features might also be useful for solar neutrino studies, which should be further explored in the future.

References

- [1] E. L. Fireman, Phys. Rev. **74**, 1238 (1948)
- [2] S. Abe *et al.* (KamLAND-Zen Collaboration), Phys. Rev. Lett. **130**, 051801 (2023), arXiv:2203.02139
- [3] M. Agostini *et al.* (GERDA Collaboration), Phys. Rev. Lett. **125**, 252502 (2020), arXiv:2009.06079
- [4] M. Agostini, G. Benato, and J. Detwiler, Phys. Rev. D **96**, 053001 (2017), arXiv:1705.02996
- [5] M. Agostini *et al.*, Rev. Mod. Phys. **95**, 025002 (2023), arXiv:2202.01787
- [6] C. Adams *et al.* (NEXT Collaboration), JHEP **2021**, 164 (2021), arXiv:2005.06467
- [7] X. Chen, *et al.*, Sci. China Phys. Mech. Astron. **60**, 061011 (2017), arXiv:1610.08883
- [8] D. R. Nygren *et al.*, JINST **13**, P03015 (2018), arXiv:1801.04513
- [9] Y. Mei, X. Sun, and N. Xu, Topmetal CMOS direct charge sensing plane for neutrinoless double-beta decay search in high-pressure gaseous TPC, arXiv: 2010.09226

- [10] X. Cao *et al.* (NvDEx Collaboration), *NvDEx-100 Conceptual Design Report*, arXiv: 2304.08362
- [11] I. R. Barabanov *et al.*, *Phys. Lett. A* **205**, 9 (1995)
- [12] R. S. Raghavan, *Phys. Rev. Lett.* **78**, 3618 (1997)
- [13] K. Zuber, *Phys. Lett. B* **709**, 6 (2012), arXiv:1108.2529
- [14] D. Frekers *et al.*, *Phys. Rev. C* **94**, 014614 (2016)
- [15] Y. Fujita, K. Zuber, and H. Fujita, *Phys. Rev. D* **104**, 013004 (2021)
- [16] G. D. O. Gann, K. Zuber, D. Bemmerer *et al.*, *Ann. Rev. Nucl. Part. Sci.* **71**, 491 (2021), arXiv:2107.08613
- [17] N. S. Phan *et al.*, *JINST* **12**, P02012 (2017), arXiv:1609.05249
- [18] M. Battaglieri *et al.*, *US Cosmic Visions: New Ideas in Dark Matter 2017: Community Report*, in *U.S. Cosmic Visions: New Ideas in Dark Matter*, 2017, arXiv: 1707.04591
- [19] C. Eldridge *et al.*, *JINST* **18**, P08021 (2023)
- [20] H. Ejiri and S. R. Elliott, *Phys. Rev. C* **95**, 055501 (2017), arXiv:1703.06915
- [21] N. Vinyoles *et al.*, *Astrophys. J.* **835**, 202 (2017), arXiv:1611.09867
- [22] J. N. Bahcall, A. M. Serenelli, and S. Basu, *Astrophys. J. Suppl.* **165**, 400 (2006), arXiv:astro-ph/0511337
- [23] A. M. Serenelli, W. C. Haxton, and C. Pena-Garay, *Astrophys. J.* **743**, 24 (2011), arXiv:1104.1639
- [24] X.-J. Xu, Z. Wang, and S. Chen, *Prog. Part. Nucl. Phys.* **131**, 104043 (2023), arXiv:2209.14832
- [25] I. Esteban *et al.*, *JHEP* **09**, 178 (2020), arXiv:2007.14792
- [26] I. Esteban *et al.*, *Nufit 5.2 (2022)*, <http://www.nu-fit.org>, accessed in July 2023.
- [27] H. Ejiri and S. R. Elliott, *Phys. Rev. C* **89**, 055501 (2014), arXiv:1309.7957
- [28] J. Allison *et al.*, *Nucl. Instrum. Meth. A* **835**, 186 (2016)
- [29] J. Allison *et al.*, *IEEE Trans. Nucl. Sci.* **53**, 270 (2006)
- [30] S. Agostinelli *et al.* (GEANT4 Collaboration), *Nucl. Instrum. Meth. A* **506**, 250 (2003)
- [31] O. A. Ponkratenko, V. I. Tretyak, and Y. G. Zdesenko, *Phys. Atom. Nucl.* **63**, 1282 (2000), arXiv:nucl-ex/0104018
- [32] C. J. Martoff *et al.*, *Nucl. Instrum. Meth. A* **440**, 355 (2000)
- [33] K. Abe *et al.* (Hyper-Kamiokande Collaboration), *Hyper-Kamiokande Design Report*, arXiv: 1805.04163
- [34] G. Bellini *et al.* (Borexino Collaboration), *Phys. Rev. D* **89**, 112007 (2014), arXiv:1308.0443
- [35] A. Abusleme *et al.* (JUNO Collaboration), *Chin. Phys. C* **45**, 023004 (2021), arXiv:2006.11760
- [36] B. Aharmim *et al.* (SNO Collaboration), *Phys. Rev. D* **102**, 062006 (2020), arXiv:2007.08018
- [37] A. A. Klimenko, *Solar neutrino background in neutrinoless double beta-decay searching for experiments*, in 54th International Meeting on Nuclear Spectroscopy and Nuclear Structure, 2004, arXiv: hep-ph/0407156
- [38] N. F. de Barros and K. Zuber, *J. Phys. G* **38**, 105201 (2011), arXiv:1103.5757
- [39] J. N. Bahcall, *Rev. Mod. Phys.* **59**, 505 (1987)
- [40] C. Giunti and C. W. Kim, *Fundamentals of Neutrino Physics and Astrophysics*, (Oxford University Press, 2007)
- [41] J. N. Bahcall, M. Kamionkowski, and A. Sirlin, *Phys. Rev. D* **51**, 6146 (1995), arXiv:astro-ph/9502003
- [42] P. Ai *et al.*, *Nucl. Instrum. Meth. A* **984**, 164640 (2020), arXiv:2005.09930
- [43] M. Kekic *et al.* (NEXT Collaboration), *JHEP* **01**, 189 (2021), arXiv:2009.10783
- [44] T. Kitaguchi *et al.*, *Nucl. Instrum. Meth. A* **880**, 188 (2018)
- [45] H. Ejiri, *Phys. Rept.* **338**, 265 (2000)
- [46] L. Hayen *et al.*, *Rev. Mod. Phys.* **90**, 015008 (2018), arXiv:1709.07530
- [47] A. N. Fazliakhmetov *et al.*, *Phys. Part. Nucl.* **54**, 547 (2023)
- [48] S. R. Elliott and H. Ejiri, *AIP Conf. Proc.* **1894**, 020008 (2017), arXiv:1708.00927
- [49] X. Mougeot, *Phys. Rev. C* **91**, 055504 (2015)
- [50] J. W. Beeman *et al.* (LUCIFER Collaboration), *Eur. Phys. J. C* **75**, 591 (2015), arXiv:1508.01709
- [51] M. An *et al.*, *Nucl. Instrum. Meth. A* **810**, 144 (2016), arXiv:1509.08611